



 Cite this: *RSC Adv.*, 2019, 9, 41540

# One-pot synthesis of Cu<sub>2</sub>O/C@H-TiO<sub>2</sub> nanocomposites with enhanced visible-light photocatalytic activity

 Aoqun Jian,<sup>ab</sup> Meiling Wang,<sup>ab</sup> Leiyang Wang,<sup>ab</sup> Bo Zhang,<sup>ab</sup> Shengbo Sang <sup>\*ab</sup> and Xuming Zhang<sup>\*c</sup>

As an environment-friendly semiconductor, titanium dioxide (TiO<sub>2</sub>), which can effectively convert solar energy to chemical energy, is a crucial material in solar energy conversion research. However, it has several technical limitations for environment protection and energy industries, such as low photocatalytic efficiency and a narrow spectrum response. In this study, a unique mesoporous Cu<sub>2</sub>O/C@H-TiO<sub>2</sub> nanocomposite is proposed to solve these issues. Polystyrene beads ((C<sub>6</sub>H<sub>8</sub>)<sub>n</sub>, PS) are utilized as templates to prepare TiO<sub>2</sub> hollow microspheres. Cu<sub>2</sub>O nanocomposites and amorphous carbon are deposited by a one-pot method on the surface of TiO<sub>2</sub> hollow spheres. After the heterojunction is formed between the two semiconductor materials, the difference in energy levels can effectively separate the photogenerated e<sup>-</sup>-h<sup>+</sup> pairs, thereby greatly improving the photocatalytic efficiency. Furthermore, due to the visible band absorption of Cu<sub>2</sub>O, the absorption range of the prepared nanocomposites is expanded to the whole solar spectrum. Amorphous carbon, as a Cu<sub>2</sub>O reduction reaction concomitant product, can further improve the electron conduction characteristics between Cu<sub>2</sub>O and TiO<sub>2</sub>. The structure and chemical composition of the obtained nanocomposites are characterized by a series of techniques (such as SEM, EDS, TEM, XRD, FTIR, XPS, DRS, PL, MS etc.). The experimental results of the degradation of methylene blue (MB) aqueous solution demonstrate that the degradation efficiency of Cu<sub>2</sub>O/C@H-TiO<sub>2</sub> nanocomposites is about 3 times as fast as that of pure TiO<sub>2</sub> hollow microspheres, and a more absolute degradation can be achieved. Herein, a recyclable photocatalyst with high degradation efficiency and a whole solar spectrum response is proposed and fabricated, and would find useful applications in environment protection, and optoelectronic devices.

 Received 25th September 2019  
 Accepted 9th December 2019

DOI: 10.1039/c9ra07767g

[rsc.li/rsc-advances](http://rsc.li/rsc-advances)

## Introduction

Due to population growth and the gradual reduction of fresh-water resources, sewage treatment is an urgent issue for human society. In recent years, the application of semiconductor oxide nanostructures as photocatalysts has been considered to be a hot research topic and has demonstrated great advantages in the treatment of contaminants in water.<sup>1,2</sup> As a kind of metal oxide semiconductor that is nontoxic, abundant, stable and photoactive, titanium dioxide (TiO<sub>2</sub>) has been widely used in the purification of water and air.<sup>3-7</sup> More and more attention has recently focused on ordered mesoporous TiO<sub>2</sub> frameworks with

high volume crystallinity and high thermal stability.<sup>8</sup> The mesoporous structure promotes the diffusion of reactants and products, and photocatalytic activities by promoting reaction sites on the surface of the photocatalyst. Furthermore, compared with the separated individual nanoparticles, mesoporous TiO<sub>2</sub> may increase the recovery efficiency of the catalyst due to its continuous particle framework.<sup>9</sup> However, TiO<sub>2</sub> nanoparticles tend to agglomerate and are difficult to achieve a solid combination by simple mixing, which increases the possibility of recombination of e<sup>-</sup>-h<sup>+</sup> pairs and is not conducive for the migration of photogenerated carriers. In recent years, the excellent properties of TiO<sub>2</sub> hollow microspheres, with low density, high surface area, excellent surface permeability and high light-harvesting efficiency, are of interest to researchers.<sup>6,10-15</sup> The large surface area provides more adsorption and reactive sites for photocatalytic reactions. The mesoporous hollow framework structure can not only promote the rapid transportation of the transmission medium, but also improve the multi-light scattering/reflection to enhance the absorption rate of light and further enhance the photocatalysis.<sup>16-18</sup>

<sup>a</sup>MicroNano System Research Center, College of Information and Computer, Taiyuan University of Technology, Taiyuan 030024, China. E-mail: jianaqun@tyut.edu.cn; mlwang\_001@163.com; wangleiyang@boe.com.cn; zhangbo0351@163.com; sunboa-sang@tyut.edu.cn

<sup>b</sup>Key Laboratory of Advanced Transducers and Intelligent Control System, Shanxi Province and Ministry of Education, Taiyuan University of Technology, Taiyuan 030024, China

<sup>c</sup>Department of Applied Physics, Hong Kong Polytechnic University, Hung Hom, Kowloon, Hong Kong, China. E-mail: xuming.zhang@polyu.edu.hk



On the other hand, due to its wide band gap (usually  $>3$  eV) of  $\text{TiO}_2$ , only ultraviolet light is absorbed and employed for photocatalyst (wavelength  $< 400$  nm, representing a maximum of 5% of energy of the solar spectrum).<sup>19,20</sup> To take full advantage of natural solar energy, a straightforward motive is to develop visible-light-responsive photocatalytic materials and further increase the energy conversion rate. For example, noble metal-supported semiconductor composites can enhance absorption in the visible region by utilizing the localized surface plasmon resonance (LSPR) effect of the metal nanoparticles, and the Schottky junction at the contact interface can suppress electron-hole recombination.<sup>21–25</sup> However, the complicated preparation process and high cost of noble metal nanostructure prohibits its widespread applications as an environmental treatment agent.<sup>19,26</sup>

At present, the heterojunctions formed by metal oxides with a suitable band structure and  $\text{TiO}_2$  are rising as a superior alternative. Cuprous oxide ( $\text{Cu}_2\text{O}$ ) is a common p-type semiconductor material with a direct band gap of 2.17 eV.<sup>21</sup> Due to its absorption of the visible band light,  $\text{Cu}_2\text{O}$  nanostructures have many applications in environmental protection, energy development and organic synthesis.<sup>27–29</sup> Wang *et al.* prepared composites of cuprous oxide ( $\text{Cu}_2\text{O}$ )/RGO with high photocatalytic performances.<sup>30</sup> Tang *et al.* studied an efficient visible-driven photocatalysts of  $\text{Cu}_2\text{O}/\text{SiNW}$  arrays.<sup>31</sup> Li *et al.* used a low temperature full solution method to prepare a ternary  $\text{ZnO}/\text{Cu}_2\text{O}/\text{Si}$  nanowire array with vertical regularity.<sup>32</sup> Experimental studies have shown that these nanostructures  $\text{Cu}_2\text{O}$  (such as rhombic dodecahedra, nanoflower shape) can be uniformly dispersed on  $\text{TiO}_2$  nanosheets to form heterojunctions. Such structures facilitate charge transfer across the interface and can achieve high catalytic activity and good catalytic durability.<sup>33</sup>

In this paper, a novel one-pot method to fabricate mesoporous hollow  $\text{Cu}_2\text{O}/\text{C}@/\text{H-TiO}_2$  structured composites is proposed. The  $\text{Cu}_2\text{O}$  nanocomposites can not only broaden the light absorption range of the composite catalyst, but also separate the  $e^-$ - $h^+$  pairs by utilizing the difference in energy band of  $\text{TiO}_2$ . On the other hand, the amorphous carbon layer on the composite catalyst can improve the electronic conductivity in the catalyst, thereby making the composite photocatalyst has a higher photocatalytic efficiency. According to the previous research,<sup>34,35</sup> a schematic diagram of the separation and transport of photogenerated charge carriers on  $\text{Cu}_2\text{O}/\text{C}@/\text{H-TiO}_2$  is schematically shown in Fig. 1a. The unique  $\text{Cu}_2\text{O}/\text{C}@/\text{H-TiO}_2$  composite material in hollow structure, improving the adsorption of pollutants and the efficiency of solar energy absorption, will have great application potential for wastewater treatment, air purification and water splitting.

The synthetic route of  $\text{Cu}_2\text{O}/\text{C}@/\text{H-TiO}_2$  photocatalyst is shown in Fig. 1b. First, tetrabutyl titanate (TBOT) is electrostatically adsorbed onto polystyrene beads ( $(\text{C}_8\text{H}_8)_n$ , PS) and then calcined to form  $\text{TiO}_2$  hollow microspheres. Next, the amorphous carbon and  $\text{Cu}_2\text{O}$  nanocomposites coatings are hydrothermally synthesized onto the  $\text{TiO}_2$  hollow microspheres by a one-pot process. The loss of the samples can be significantly reduced by simplification of the preparation steps.

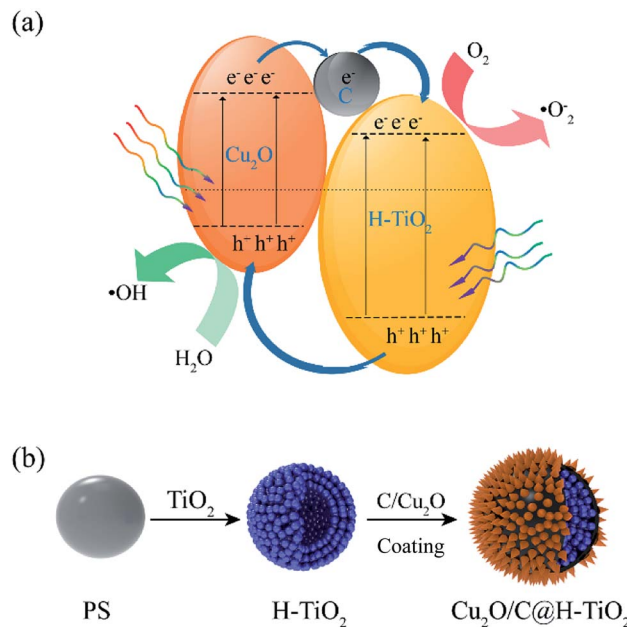


Fig. 1 (a) Schematic diagram for photogenerated charge carriers separation and transportation, (b) synthesis route of  $\text{Cu}_2\text{O}/\text{C}@/\text{H-TiO}_2$  spherical photocatalyst.

## Experiment

Reagents:  $\text{C}_6\text{H}_{12}\text{O}_6$ ;  $\text{CuCl}_2 \cdot 2\text{H}_2\text{O}$ , NaOH, polystyrene beads ( $(\text{C}_8\text{H}_8)_n$ , PS); tetrabutyl titanate ( $\text{C}_{16}\text{H}_{36}\text{O}_4\text{Ti}$ , TBOT), ammonia ( $\text{NH}_3 \cdot \text{H}_2\text{O}$ ), ethyl alcohol absolute ( $\text{C}_2\text{H}_5\text{OH}$ ), acetonitrile ( $\text{C}_2\text{H}_3\text{N}$ ), deionized water was used for all experiments.

### Synthesis of hollow $\text{TiO}_2$ microspheres

Refer to previous research results,<sup>36</sup>  $\text{H-TiO}_2$  microspheres were prepared according to the electrostatic adsorption and calcination methods, in which 0.024 g polystyrene (PS) beads were added into a mixture solution containing 75 mL ethanol, 25 mL acetonitrile and 300  $\mu\text{L}$  ammonia to configure solution A under vigorous stirring for 3 h. 0.5 mL TBOT was added into a mixture solution containing 15 mL ethanol and 5 mL acetonitrile to configure solution B. After stirring for 5 min, the solution B was slowly added dropwise to the solution A, and the ultimately solution were isolated by centrifugation and washed with ethanol and deionized water to obtain  $\text{TiO}_2@/\text{PS}$  microspheres. The powder were dispersed in a reaction kettle containing deionized water at 80  $^\circ\text{C}$  for 24 h, then centrifuged and dried at 80  $^\circ\text{C}$ . The  $\text{TiO}_2$  hollow microspheres ( $\text{H-TiO}_2$ ) were obtained by calcining the dried powder in a muffle furnace at 400  $^\circ\text{C}$  for 4 h.

### Synthesis of $\text{Cu}_2\text{O}/\text{C}@/\text{H-TiO}_2$ microspheres

Three different qualities of  $\text{CuCl}_2 \cdot 2\text{H}_2\text{O}$  were dispersed in three beakers with 20 mL of deionized water, respectively. The corresponding  $\text{H-TiO}_2$  microspheres and a certain amount of NaOH were then added to the  $\text{CuCl}_2 \cdot 2\text{H}_2\text{O}$  solution by magnetic stirring for 1 h. Then  $\text{C}_6\text{H}_{12}\text{O}_6 \cdot \text{H}_2\text{O}$  was dispersed into the green suspension during stirring. The resulting suspension was



transferred to a 50 mL polytetrafluoroethylene lined stainless steel autoclave. The hydrothermal treatment was carried out at 100 °C for 8 h. The product was collected and washed several times with deionized water and ethanol and dried in vacuum at 80 °C to prepare 4 wt%, 8 wt% and 20 wt% Cu<sub>2</sub>O/C@H-TiO<sub>2</sub> microspheres.

## Characterization

The morphology of the synthesized product was investigated using a scanning electron microscope (SEM) images and energy dispersive spectroscopy (EDS), which were acquired with a Hitachi model SU8010. The crystalline phase and the phase purity of the samples was recorded by high-resolution transmission electron microscopy (HR-TEM, JEM-1400 plus) and X-ray diffraction (XRD, Rigaku-D/max-2500) within  $2\theta$  range from 20° to 80° by using a Cu K $\alpha$  radiation. UV-vis diffuse reflectance spectroscopy (DRS) of the samples were retrieved from a UV-2600 spectrophotometer with an integrating sphere accessory in the range of 300 to 800 nm. The X-ray photoelectron spectroscopy (XPS) spectra were performed on Thermo ESCALAB 250XI System to determine the chemical status of the as-prepared Cu<sub>2</sub>O/C@H-TiO<sub>2</sub> microspheres. N<sub>2</sub> adsorption-desorption isotherms were measured on a Micromeritics BK122W automatic adsorption instrument at 120 °C for 8 h. Fourier-transform infrared (FTIR) spectra were evaluated using a Bruker Vector 33 FT-IR spectrophotometer in the range of 4000–400 cm<sup>-1</sup> with a resolution of 4 cm<sup>-1</sup> using the conventional KBr pellet technique. Photoluminescence (PL) spectra and time resolved photoluminescence spectra (TRPL) were recorded on a fluorescence spectrometer (FLS 980-STM, Edinburgh instruments).

The three-electrode system was immersed in 0.5 M Na<sub>2</sub>SO<sub>4</sub> in which the sample was prepared on a ITO glass as a working electrode, a platinum plate as a counter electrode, and a saturated calomel electrode as a reference electrode to evaluate photoelectric properties.

The methylene blue (MB) aqueous solution of 20 mg L<sup>-1</sup> was photodegraded in a 500 mL quartz photoreactor at 25 °C. The photocatalyst of 20 mg was dispersed in a 50 mL MB solution, and stirred for 30 min in a dark environment to establish an adsorption-desorption equilibrium, followed by irradiation with a Xe lamp (300 nm <  $\lambda$  < 1100 nm) for photocatalytic reaction. The sample was sampled every 10 min under the conditions of constant temperature of circulating water. After removing the catalyst by centrifugation, the supernatant was measured for absorbance using an UV-vis spectrophotometer (Cary 100, Varian) on photodegradation at 662 nm to obtain the degradation rate. Finally, the catalytic efficiencies of the synthesized catalysts were summarized and compared.

## Results and discussion

Fig. 2 presents the corresponding SEM and HR-TEM images and EDS analysis monitoring the formation of as prepared H-TiO<sub>2</sub> microspheres and Cu<sub>2</sub>O/C@H-TiO<sub>2</sub> microspheres. It can be seen from Fig. 2a that the PS spheres are regular and uniform

spheres with an average diameter of about 4.56  $\mu$ m. The fabricated core-shell microspheres PS@TiO<sub>2</sub> is shown in Fig. 2b. The surface of the microspheres become a little bit rough. The particle size is obviously enlarged (about 5.22  $\mu$ m), indicating that TiO<sub>2</sub> layer is indeed deposited on the surface of the template polymer PS, and the thickness of coated TiO<sub>2</sub> layer is about 0.11  $\mu$ m. After further calcination, the PS pellets are burned and decomposed, only TiO<sub>2</sub> shells are left behind. The TiO<sub>2</sub> shells shrink obviously after further crystallization. The average particle size of the hollow microspheres is about 3.97  $\mu$ m (in Fig. 2c). A distinct hollow structure can be observed by crushing the calcined H-TiO<sub>2</sub> microspheres with tweezers (inset in Fig. 2c). During the calcination of PS@TiO<sub>2</sub> core-shell microspheres, the sample quickly loses a large amount of water in a short time. Some spheres are likely to collapse with the rapid disappearance of PS. Therefore, the heating rate of the calcination temperature and the pre-high temperature treatment before the calcination are elaborated to enhance the product yield of TiO<sub>2</sub> sphere shells. The fabricated Cu<sub>2</sub>O/C@H-TiO<sub>2</sub> microspheres are presented in Fig. 2d and e. Compared with the H-TiO<sub>2</sub> microspheres, the average diameter of Cu<sub>2</sub>O/C@H-TiO<sub>2</sub> microspheres is about 4.80  $\mu$ m, and the surface of the spheres becomes rougher. The EDS analysis offered in Fig. 2f confirms that the elements C, O, Ti, Cu exist on the surface of the microspheres. In order to further analyze the interface structure and material composition, a high-resolution transmission electron microscope (HR-TEM) image of the Cu<sub>2</sub>O/C@H-TiO<sub>2</sub> composite is presented in Fig. 2g. The lattice distances of 0.25 nm and 0.35 nm in the figure correspond to the (111) and (101) planes of Cu<sub>2</sub>O and TiO<sub>2</sub>, respectively.<sup>37</sup> This shows the well-developed interfaces between Cu<sub>2</sub>O and the TiO<sub>2</sub>. In addition, a carbon with a lattice spacing of 0.34 nm is also detected here. This is part of the product produced during the dehydration and polycondensation of glucose molecules.

Fig. 3a shows the crystal structure of the H-TiO<sub>2</sub>, 4 wt% Cu<sub>2</sub>O/C@H-TiO<sub>2</sub>, 8 wt% Cu<sub>2</sub>O/C@H-TiO<sub>2</sub>, 20 wt% Cu<sub>2</sub>O/C@H-TiO<sub>2</sub> by XRD patterns. As can be seen all the diffraction peaks of the samples at  $2\theta = 25.267^\circ, 37.702^\circ, 47.975^\circ, 53.912^\circ, 54.966^\circ, 62.640^\circ, 68.809^\circ, 70.274^\circ, 75.116^\circ$  are corresponding to anatase TiO<sub>2</sub>, indexed very well to JCPDS card no. 21-1272.<sup>38,34</sup> But no obvious Cu<sub>2</sub>O diffraction peaks are found in 4 wt% Cu<sub>2</sub>O/C@H-TiO<sub>2</sub>, 8 wt% Cu<sub>2</sub>O/C@H-TiO<sub>2</sub> due to the limited amount of Cu<sub>2</sub>O. However, for 20 wt% Cu<sub>2</sub>O/C@H-TiO<sub>2</sub>, the peaks of Cu<sub>2</sub>O can be observed at  $2\theta = 29.581^\circ, 36.413^\circ, 42.352^\circ, 61.383^\circ, 73.525^\circ, 77.366^\circ$ .<sup>29</sup> In addition, with the increase of the amount of Cu<sub>2</sub>O and carbon, a diffraction peak about graphitic carbon is detected at a position of about  $2\theta = 27.4^\circ$ . This is consistent with the HR-TEM results, which indicates that a small amount of graphitic carbon is formed in the amorphous carbon.<sup>38</sup> The Fourier-transform IR (FTIR) spectra of samples are presented in Fig. 3b. The broad absorption peak at approximately 3420 cm<sup>-1</sup> band can be assigned to O-H stretching vibration in the alcohol group as well as the intercalated or adsorbed water molecules in the samples.<sup>39,40</sup> The signal at 700 cm<sup>-1</sup> is characteristic of the O-Ti-O lattice formation. The peak value of 1632 cm<sup>-1</sup> is attributed to the surface -OH or water bending mode of the four samples. The peak of 623 cm<sup>-1</sup> is corresponded to the



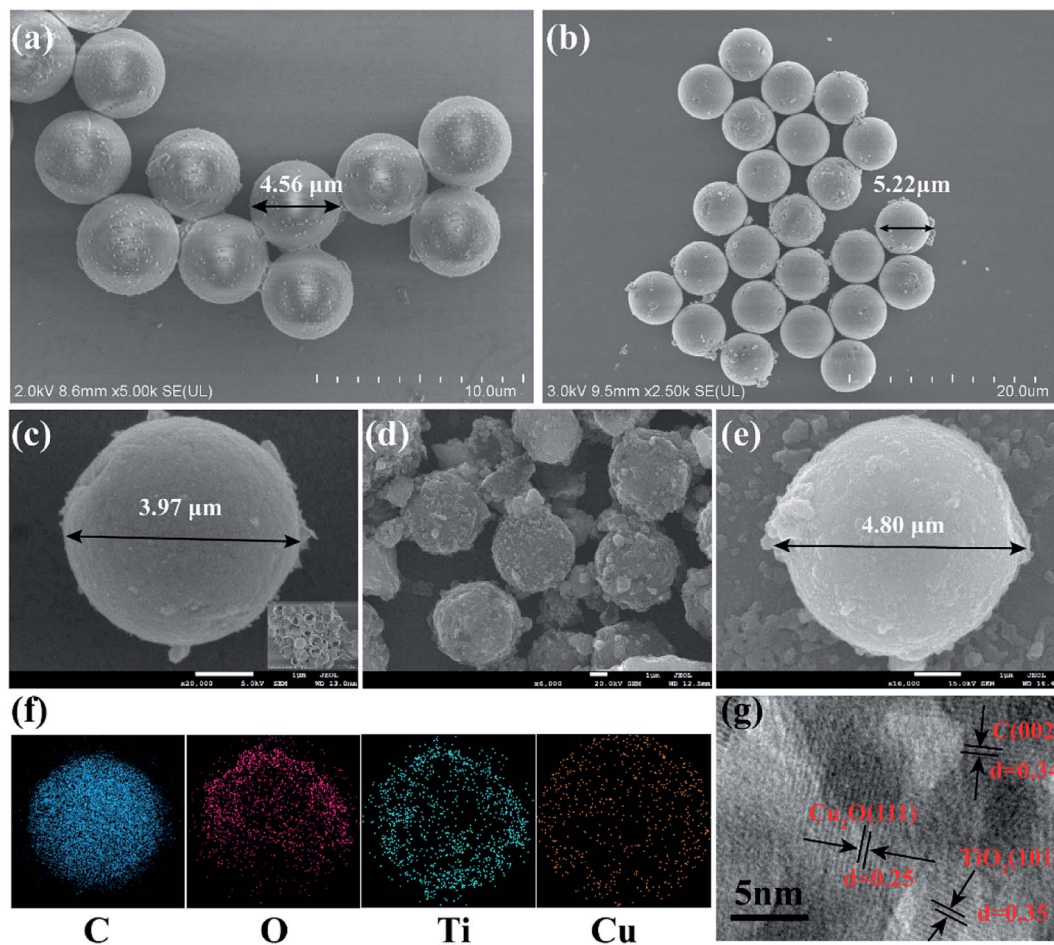


Fig. 2 The SEM images of (a) PS spheres, (b) PS@TiO<sub>2</sub> microspheres, (c) hollow TiO<sub>2</sub> (H-TiO<sub>2</sub>) microspheres, (d and e) Cu<sub>2</sub>O/C@H-TiO<sub>2</sub> microspheres, (f) the EDS images of Cu<sub>2</sub>O/C@H-TiO<sub>2</sub> microspheres, (g) HR-TEM images on Cu<sub>2</sub>O/C@H-TiO<sub>2</sub>.

stretching of copper(I)-O bond in Cu<sub>2</sub>O/C@H-TiO<sub>2</sub>, indicating the formation of Cu<sub>2</sub>O.<sup>40</sup> This observation is consistent well with the results obtained by SEM, EDS, XRD and HR-TEM.

To further explore the composition and chemical state of elements in Cu<sub>2</sub>O/C@H-TiO<sub>2</sub> samples, X-ray photoelectron spectroscopy (XPS) analysis is conducted and illustrated in

Fig. 4. The survey spectrum (Fig. 4a) demonstrates that the Cu<sub>2</sub>O/C@H-TiO<sub>2</sub> samples contain C, O, Ti and Cu element. More specifically, as presented in Fig. 4b, the high-resolution of Ti2p shows two peaks at binding energies of 463.8 eV and 461.5 eV, corresponding to Ti2p<sub>1/2</sub> and Ti2p<sub>3/2</sub> spin-orbital splitting photoelectrons. Separation between Ti2p<sub>1/2</sub> and

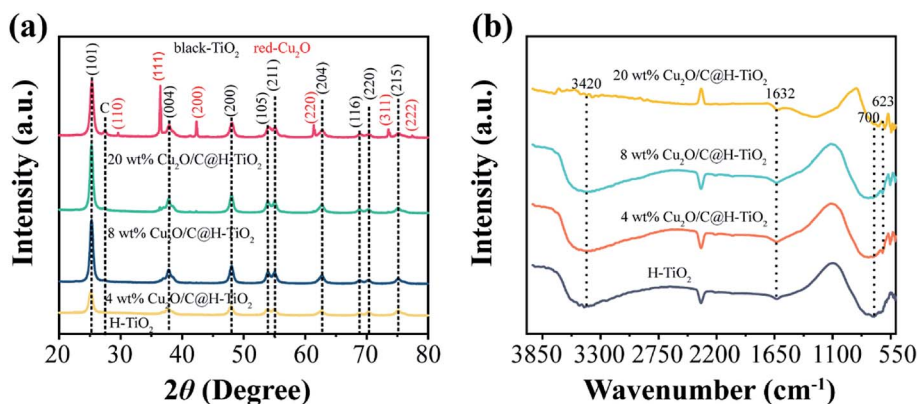


Fig. 3 XRD patterns (a) and FTIR spectra (b) of the photocatalysts.



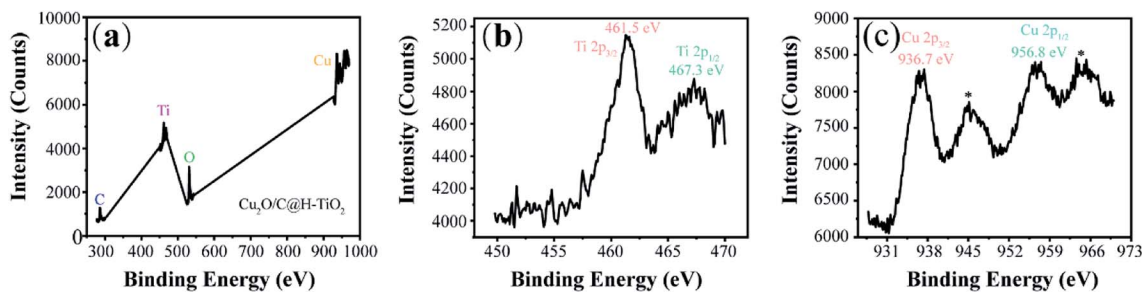


Fig. 4 (a) The XPS images of  $\text{Cu}_2\text{O}/\text{C}@H\text{-TiO}_2$  microspheres. Fine scan XPS spectra of (b)  $\text{Cu}2p$ ; (c)  $\text{Ti}2p$  of  $\text{Cu}_2\text{O}/\text{C}@H\text{-TiO}_2$  microspheres.

$\text{Ti}2p_{3/2}$  (approximately 6.0 eV) suggests a normal state of  $\text{Ti}^{4+}$  in the  $\text{Cu}_2\text{O}/\text{C}@H\text{-TiO}_2$  microspheres.<sup>2,41</sup> Fig. 4c demonstrates the high-resolution XPS spectrum  $\text{Cu}2p$  of 936.7 and 956.8 eV assigned to  $\text{Cu}2p_{3/2}$  and  $\text{Cu}2p_{1/2}$ , respectively. Notably, according to previous reports,<sup>34</sup> the binding energy of  $\text{Cu}^+$  is located at 934 and 952.5 eV, therefore, the measured  $\text{Cu}2p$  binding energy may be the result of an adjustment synergy between the heterojunction structure between  $\text{Cu}_2\text{O}$  and  $\text{TiO}_2$  and the amorphous carbon doping.<sup>19,37,42</sup>

The Fig. 5 indicates the  $\text{N}_2$  adsorption–desorption isotherms and pore size distributions of  $\text{H-TiO}_2$  and  $\text{Cu}_2\text{O}/\text{C}@H\text{-TiO}_2$ . According to the 1985 IUPAC classification, both isotherms show type IV adsorption isotherms and  $\text{H}_2$  type hysteresis loops.<sup>8,43</sup> The adsorption/desorption curves are plotted in orange and blue respectively. Since these two curves are not closed, the hysteresis loop demonstrates that the synthesized material is mesoporous. It can be seen that the specific surface area of  $\text{Cu}_2\text{O}/\text{C}@H\text{-TiO}_2$  is smaller than that of  $\text{H-TiO}_2$ . The reduction in surface area may indicate the adsorption of amorphous carbon and  $\text{Cu}_2\text{O}$  within the mesopores, which causes the partial loss of mesoporosity. The BJH desorption pore size distribution are shown in the insets of Fig. 5. For  $\text{H-TiO}_2$ , the narrow pore diameters are mainly distributed at 3–10 nm, and the narrow pore size is unchanged in the case of  $\text{Cu}_2\text{O}/\text{C}@H\text{-TiO}_2$ . The results above suggest that the mesoporous structure is retained after the introduction of  $\text{Cu}_2\text{O}$  nanocomposites and amorphous carbon. It is encouraging to

find that the prepared composite material has an open mesoporous structure, which can make a fast transmission medium, provide more active sites to adsorb organic molecules, and can improve multiple light scattering/reflection to enhance light absorb.

The optical property of the composite is characterized by UV-vis diffuse reflectance spectroscopy (DRS). The absorption spectra of  $\text{H-TiO}_2$  and  $\text{Cu}_2\text{O}/\text{C}@H\text{-TiO}_2$  microsphere composites are presented in Fig. 6. All the samples have strong absorption in the ultraviolet region, which is mainly due to the absorption of  $\text{H-TiO}_2$ . Compared with pure  $\text{H-TiO}_2$  spheres, the  $\text{Cu}_2\text{O}/\text{C}@H\text{-TiO}_2$  nanocomposites samples have a stronger absorption spectrum in the visible range. This may be attributed to the presence of amorphous carbon and  $\text{Cu}_2\text{O}$  in the nanocomposites. In  $\text{Cu}_2\text{O}/\text{C}@H\text{-TiO}_2$  nanocomposites,  $\text{Cu}_2\text{O}$  can absorb visible light and promote the separation of photo-generated  $e^-h^+$  pairs by forming a heterojunction with  $\text{H-TiO}_2$ . However, when the compounding amount increases to 20 wt% by weight, the absorbance is not significantly improved, which may be because an excessive amount of compounding will bring about a new carrier recombination center, or an excessive amount of  $\text{Cu}_2\text{O}$  and amorphous carbon will affect the adjustment of light in the mesoporous hollow structure, thereby reducing light absorption. According to the absorption spectra of the photocatalysts, the band gap energy of all photocatalysts can be derived from the relationship between light energy ( $\alpha h\nu$ )<sup>2</sup> and photon energy  $h\nu$  (in the Fig. 6b). The band gap energies of

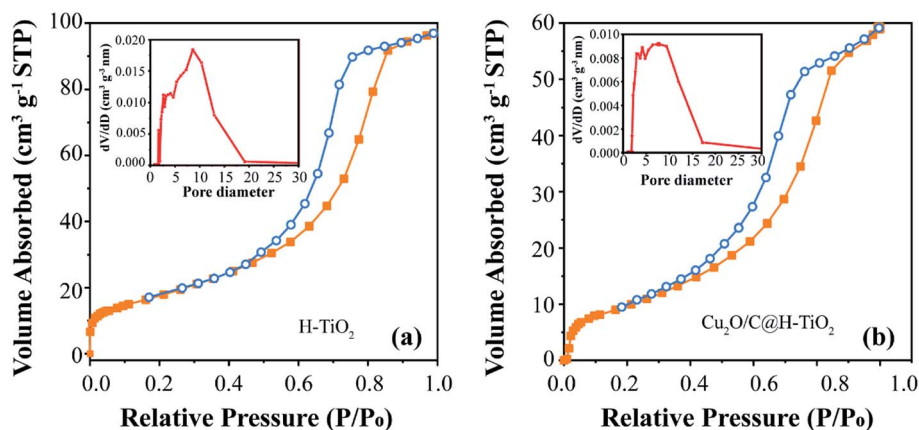


Fig. 5  $\text{N}_2$  physisorption isotherms (a) of  $\text{H-TiO}_2$ , (b) of  $\text{Cu}_2\text{O}/\text{C}@H\text{-TiO}_2$ .



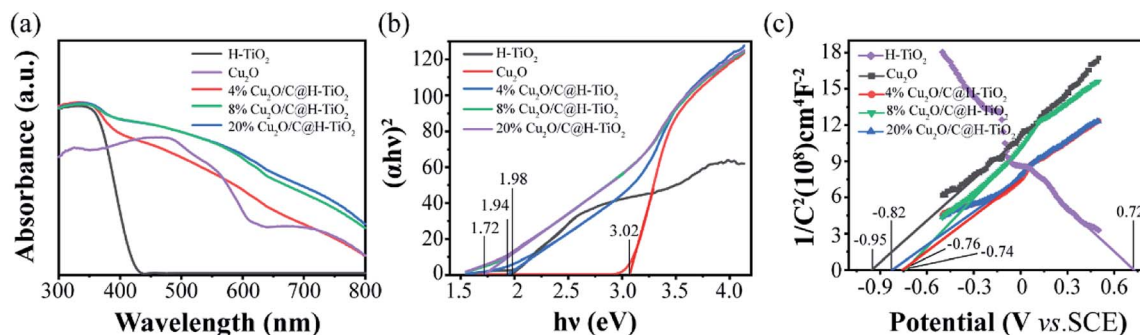


Fig. 6 (a) UV-vis absorption spectra of all the samples, (b) Tauc plots calculated from (a), (c) Mott–Schottky plots measured under 1000 Hz of the photoanodes.

H-TiO<sub>2</sub>, Cu<sub>2</sub>O, 4 wt%, 8 wt%, and 20 wt% Cu<sub>2</sub>O/C@H-TiO<sub>2</sub> are calculated to be 3.02, 1.98, 1.94, 1.72, and 1.72 eV, respectively. And the  $E_g$  of Cu<sub>2</sub>O/C@H-TiO<sub>2</sub> nanocomposites are smaller than H-TiO<sub>2</sub>. The narrowing of the bandgap  $E_g$  may be due to electron transfer transition between H-TiO<sub>2</sub>, Cu<sub>2</sub>O and amorphous carbon (see Fig. 1a). Therefore, it can be inferred that nanocomposites photocatalyst Cu<sub>2</sub>O/C@H-TiO<sub>2</sub> can absorb visible light more effectively and may have higher photocatalytic activity than pure H-TiO<sub>2</sub>.

The Mott–Schottky (MS) patterns of the nanocomposites are measured to investigate its flat band potential and charge density,<sup>44–50</sup> as shown in Fig. 6c. The H-TiO<sub>2</sub> and other Cu<sub>2</sub>O/C@H-TiO<sub>2</sub> nanocomposites materials show typical n-type positive slopes, and Cu<sub>2</sub>O is a p-type negative slope. The charge density ( $N_d$ ) is achieved based on following formula:

$$N_d = (2/\epsilon_0\epsilon)[d(1/C^2)/dV]^{-1} \quad (1)$$

where  $e$ ,  $\epsilon_0$ ,  $\epsilon$  represent the electron charge, vacuum permittivity and dielectric constant of H-TiO<sub>2</sub>, respectively. The obtained charge density of H-TiO<sub>2</sub>, 4 wt%, 8 wt% and 20 wt% Cu<sub>2</sub>O/C@H-TiO<sub>2</sub> by linear fit slopes are  $1.42 \times 10^{21}$ ,  $1.67 \times 10^{21}$ ,  $1.78 \times 10^{21}$  and  $1.21 \times 10^{21} \text{ cm}^{-3}$ , respectively. As the Cu<sub>2</sub>O and amorphous carbon doping concentration grew from 0 wt% to 8 wt%, an increase in charge density and a decrease in recombination are observed. However, after the excess Cu<sub>2</sub>O and amorphous carbon are combined, the charge density may decrease, which may be due to the limitation of light absorption and the addition of new carrier recombination centers. In addition, the flat band potential of Cu<sub>2</sub>O/C@H-TiO<sub>2</sub> nanocomposites is significantly positively shifted with respect to that of the pure H-TiO<sub>2</sub>, and the corresponding band gaps is narrowed. Therefore, an appropriate amount of Cu<sub>2</sub>O and amorphous carbon results in a decrease in the band bending edge at the junction with H-TiO<sub>2</sub> and an increase in the carrier density in the catalytic system.

To further understand the charge transfer in all samples, photoluminescence spectroscopy (PL) measurements are concluded at room temperature.<sup>51</sup> Fig. 7a shows the steady state PL spectrum of all samples collected at an excitation wavelength of 270 nm. It can be seen that the PL intensity of the Cu<sub>2</sub>O/C@H-TiO<sub>2</sub> samples are greatly suppressed compared with pure H-TiO<sub>2</sub> and Cu<sub>2</sub>O samples, indicating decreasing the

recombination rate of the photogenerated carriers. Significantly, the PL intensity gradually decreased as the loaded amount of Cu<sub>2</sub>O and amorphous carbon increased from 0 wt% to 8 wt%, and then rose further increased to 20 wt%. This indicates that introduction of Cu<sub>2</sub>O and amorphous carbon in an appropriate amount results in a decrease in charge recombination rate, and more photogenerated carriers may be transported to the surface of the photocatalyst to participate in the photocatalytic reaction. The higher PL strength of 20 wt% Cu<sub>2</sub>O/C@H-TiO<sub>2</sub> may be due to the recombination center of the carriers introduces by the loading of excess Cu<sub>2</sub>O and amorphous carbon. In addition, time resolved photoluminescence spectroscopy (TRPL) measurements are also performed, as shown in Fig. 7b. The 8 wt% Cu<sub>2</sub>O/C@H-TiO<sub>2</sub> nanocomposites shows the longest decay time (0.567 ns) in all samples after fitting the curve with the exponential model, indicating a lower recombination rate of generated  $e^-h^+$  pairs. These results are consistent well with the DRS and MS carried out above.

In Fig. 8a, pure H-TiO<sub>2</sub> and Cu<sub>2</sub>O have lower photocurrent density values of 0.67 and 1.2  $\mu\text{A cm}^{-2}$  in a 0.5 M Na<sub>2</sub>SO<sub>4</sub> electrolyte through a three-electrode system at 0 V SCE, respectively. And they are accompanied by obvious current spikes (especially H-TiO<sub>2</sub>). This proves that they have a high photo-generated charge recombination rate. However, for the nanocomposites photocatalyst Cu<sub>2</sub>O/C@H-TiO<sub>2</sub>, the photocurrents are high and stable. This indicates that Cu<sub>2</sub>O and amorphous carbon enhances the light absorption rates in photocatalysts and promote carrier separation. When the loading is 8 wt%, the photocatalyst exhibits higher photocurrent density (5.6  $\mu\text{A cm}^{-2}$ ), which is about 8 times and 4.7 times that of pure H-TiO<sub>2</sub> and Cu<sub>2</sub>O photocatalysts, respectively. In addition, the decrease in the photocurrent of the 20 wt% Cu<sub>2</sub>O/C@H-TiO<sub>2</sub> photocatalyst indicates that excessive Cu<sub>2</sub>O and amorphous carbon loading are not conducive to effective charge separation, which is consistent with other characteristics described above.

All the photocatalysts have an obvious MB removal efficiency when they are dispersed in the solution under the light irradiation. And a blank experiment is also carried out to eliminate the self-photolysis of MB. The 8 wt% Cu<sub>2</sub>O/C@TiO<sub>2</sub> nanocomposites have better photocatalytic activity than the other photocatalysts as time passes by. Its degradation efficiency at



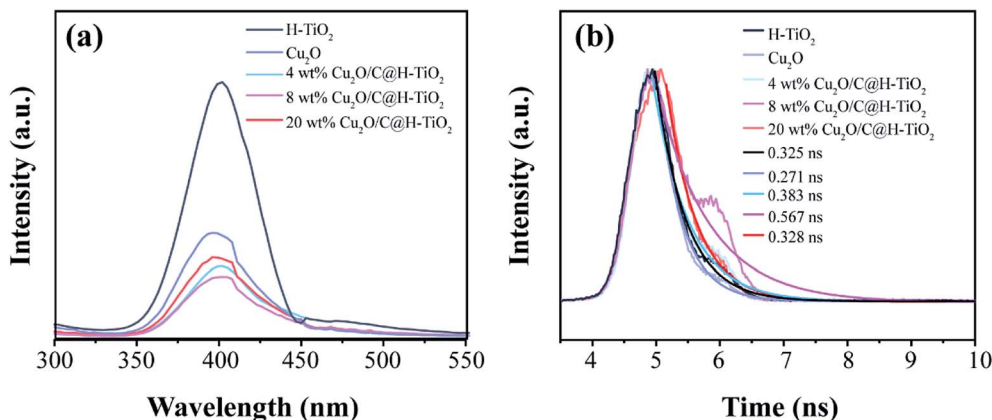


Fig. 7 (a) PL emission spectra and (b) time-resolved fluorescence spectra of all the samples.

50 min is as 3 times and 2.3 times as those of H-TiO<sub>2</sub> and 4 wt% Cu<sub>2</sub>O/C@H-TiO<sub>2</sub>, respectively, and the degradation is close to 100% at 100 min. The improvement of the photocatalytic performance of the combined nanoparticles is mainly due to the charge transition at the interface between Cu<sub>2</sub>O and TiO<sub>2</sub> with a matching band structure. Another reason attributes to the amorphous carbon particles at the interface of heterojunction improve the conduction properties of electrons, thus facilitating effective photoexcitation e<sup>-</sup>-h<sup>+</sup> separation.

As the amount of Cu<sub>2</sub>O and amorphous carbon grows from 0 wt% to 8 wt%, the catalytic performances of the composite photocatalyst gradually enhances. When the amount of Cu<sub>2</sub>O and amorphous carbon reaches 20 wt%, the photocatalytic ability drops and is even smaller than that of H-TiO<sub>2</sub>. This may be because excessive Cu<sub>2</sub>O nanocomposites will introduce new carrier recombination centers and block the pore structure of H-TiO<sub>2</sub>, which will affect the light absorption rate of H-TiO<sub>2</sub>, thus reducing the photocatalytic efficiency.

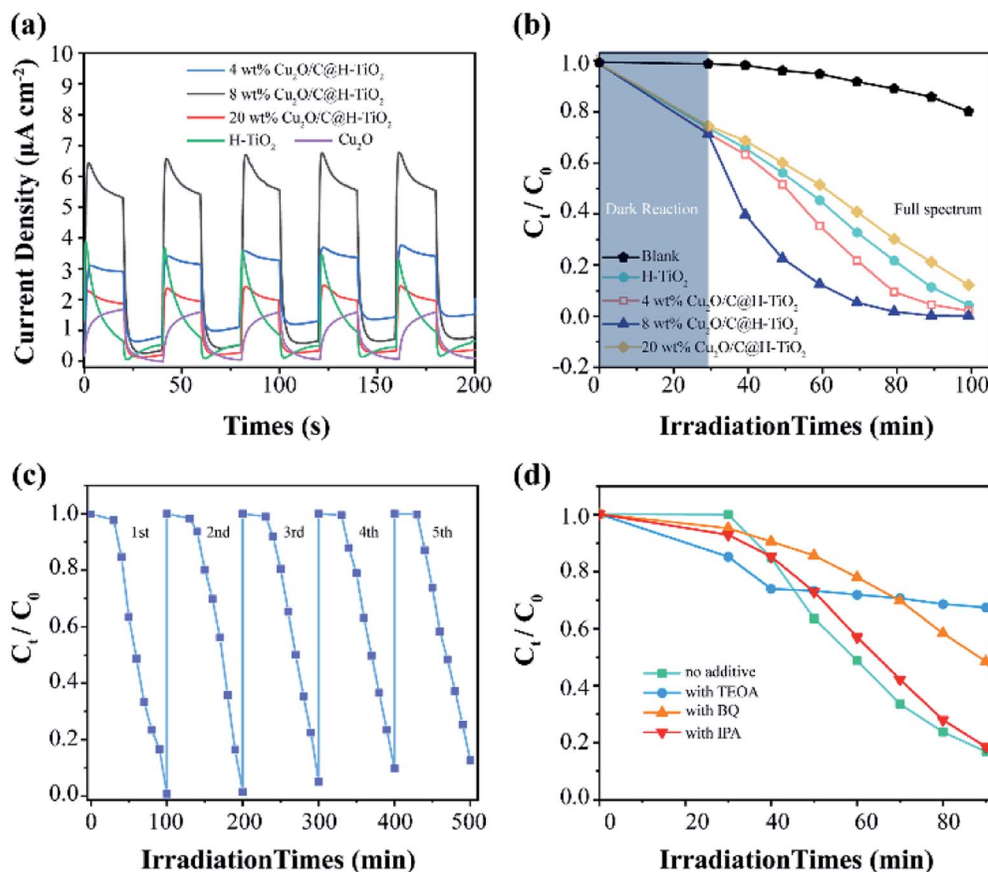


Fig. 8 (a) Current density–time ( $I-t$ ) measured in 0.5 M Na<sub>2</sub>SO<sub>4</sub> electrolyte; (b) photocatalytic degradation of MB in the presence of different prepared photocatalysts; (c) photocatalyst stability under photodegradation, and (d) catalytic activity of photocatalysts with different scavengers.



The reusability and stability of photocatalysts are crucial considerations for practical applications. Taking the 8 wt% Cu<sub>2</sub>O/C@H-TiO<sub>2</sub> photocatalyst as an example, a cycle test of MB degradation is carried out. In Fig. 8c, the photocatalytic degradation activity decreased by less than 15% after 5 cycles of the test, indicating higher light stability. The effects of various active species on the degradation of MB in this experiment are studied in Fig. 8d. Triethanolamine (TEOA, 0.01 mol L<sup>-1</sup>), isopropyl alcohol (IPA, 0.02 mol L<sup>-1</sup>), and *p*-benzoquinone (BZQ, 0.1 mmol L<sup>-1</sup>) are used as scavengers of photogenerated holes (h<sup>+</sup>), hydroxyl radical (·OH), and superoxide radicals (·O<sup>2-</sup>), respectively.<sup>52-54</sup> Meanwhile, the experiment with no scavenger under the same experimental conditions is carried out for compared. The addition of TEOA and BZQ in the experiment cause a significant decrease in photocatalytic degradation, indicating that photogenerated holes (h<sup>+</sup>), and superoxide radicals (·O<sup>2-</sup>) play a major role in the degradation of MB. Furthermore, the addition of IPA do not significantly affect the degree of degradation of MB, which means hydroxyl radical (·OH) is not the main active substance in this photocatalytic degradation.

## Conclusion and outlook

In this paper, mesoporous Cu<sub>2</sub>O/C@H-TiO<sub>2</sub> nanocomposites is proposed. Amorphous carbon and Cu<sub>2</sub>O nanocomposites are simultaneously composited onto TiO<sub>2</sub> microspheres by a one-pot reaction. The structure, crystal phase and chemical state of the composite photocatalyst are confirmed by various characterizations. The photocatalytic performance of prepared sample is tested by MB degradation, and the photocatalytic enhancement mechanism is also analyzed. It is found that the optimized loading of Cu<sub>2</sub>O nanocomposites and amorphous carbon can enhance the photocatalytic efficiency of the composite catalyst. The Cu<sub>2</sub>O nanocomposites not only broaden the light absorption range of the composite catalyst, but also separate the e<sup>-</sup>-h<sup>+</sup> pairs by utilizing the difference in energy band of the TiO<sub>2</sub>. Furthermore, the amorphous carbon particles on the composite catalyst can improve the electronic conductivity of the catalyst, thereby making the composite photocatalyst has a higher photocatalytic efficiency. Due to its significantly improved photocatalytic performance and simple preparation, the mesoporous Cu<sub>2</sub>O/C@H-TiO<sub>2</sub> nanocomposites would find useful applications in environment protection and optoelectronic devices.

## Availability of data and material

All data generated or analysed during this study are included in this published article.

## Authors' contributions

Aoqun Jian and Xuming Zhang designed the experiments; Meiling Wang and Leiyang Wang performed the experiments; Meiling Wang and Bo Zhang analyzed the data; Meiling Wang wrote the paper; Shengbo Sang and Aoqun Jian discussed the

results and commented on the manuscript. All authors read and approved the final manuscript.

## Conflicts of interest

The authors declare that they have no competing interests.

## Acknowledgements

This study was financially supported by the National Natural Science Foundation of China (No. 61971301, 51622507), 863 project (2015AA042601), Excellent Talents Technology Innovation Program of Shanxi Province (201805D211021), and Research Grants Council of Hong Kong (N\_PolyU505/13, 152184/15E, 152127/17E and 152126/18E).

## References

- 1 G. Yang, Z. Yan and T. Xiao, *Appl. Surf. Sci.*, 2012, **258**, 8704–8712.
- 2 C. Liu, D. Yang, Y. Jiao, Y. Tian, Y. Wang and Z. Jiang, *ACS Appl. Mater. Interfaces*, 2013, **5**, 3824–3832.
- 3 Y. Ma, X. Wang, Y. Jia, X. Chen, H. Han and C. Li, *Chem. Rev.*, 2014, **114**, 9987–10043.
- 4 F. X. Xiao, S. F. Hung, J. Miao, H. Y. Wang, H. Yang and B. Liu, *Small*, 2015, **11**, 554–567.
- 5 M. M. Khan, S. F. Adil and A. Al-Mayouf, *J. Saudi Chem. Soc.*, 2015, **19**, 462–464.
- 6 R. Yang, J. Cai, K. Lv, X. Wu, W. Wang, Z. Xu, M. Li, Q. Li and W. Xu, *Appl. Catal., B*, 2017, **210**, 184–193.
- 7 S. M. Gupta and M. Tripathi, *Chin. Sci. Bull.*, 2011, **56**, 1639–1657.
- 8 H. Liu, W. Li, D. Shen, D. Zhao and G. Wang, *J. Am. Chem. Soc.*, 2015, **137**, 13161–13166.
- 9 A. A. Ismail and D. W. Bahnemann, *J. Mater. Chem.*, 2011, **21**, 11686–11707.
- 10 H. Li, J. Li, Y. Zhu, W. Xie, R. Shao, X. Yao, A. Gao and Y. Yin, *Anal. Chem.*, 2018, **90**, 5496–5502.
- 11 B.-X. Lei, L.-L. Zeng, P. Zhang, X.-F. Zheng, Y.-S. Wu, J. Fu and Z.-F. Sun, *RSC Adv.*, 2014, **4**, 29099–29106.
- 12 S. Li, J. Chen, F. Zheng, Y. Li and F. Huang, *Nanoscale*, 2013, **5**, 12150–12155.
- 13 X. Jiang, C. Li, S. Liu, F. Zhang, F. You and C. Yao, *RSC Adv.*, 2017, **7**, 24598–24606.
- 14 Y. Bao, Q. L. Kang, J. Z. Ma and C. Liu, *Ceram. Int.*, 2017, **43**, 8596–8602.
- 15 J. Yu and J. Zhang, *Dalton Trans.*, 2010, **39**, 5860–5867.
- 16 B. Fang, Y. Xing, A. Bonakdarpour, S. Zhang and D. P. Wilkinson, *ACS Sustainable Chem. Eng.*, 2015, **3**, 2381–2388.
- 17 B. Fang, A. Bonakdarpour, K. Reilly, Y. Xing, F. Taghipour and D. P. Wilkinson, *ACS Appl. Mater. Interfaces*, 2014, **6**, 15488–15498.
- 18 B. Fang, J. H. Kim, M. S. Kim and J. S. Yu, *Acc. Chem. Res.*, 2012, **46**, 1397–1406.





- 19 K. Zhao, S. Zhao, J. Qi, H. Yin, C. Gao, A. M. Khattak, Y. Wu, A. Iqbal, L. Wu, Y. Gao, R. Yu and Z. Tang, *Inorg. Chem. Front.*, 2016, **3**, 488–493.
- 20 U. I. Gaya and A. H. Abdullah, *J. Photochem. Photobiol., C*, 2008, **9**, 1–12.
- 21 W.-Y. Cheng, T.-H. Yu, K.-J. Chao and S.-Y. Lu, *Int. J. Hydrogen Energy*, 2013, **38**, 9665–9672.
- 22 S. Kumar, M. Anija and A. K. Sood, *Plasmonics*, 2013, **8**, 1477–1483.
- 23 Y. Lu, H. Yu, S. Chen, X. Quan and H. Zhao, *Environ. Sci. Technol.*, 2012, **46**, 1724–1730.
- 24 S. K. Cushing, J. Li, F. Meng, T. R. Senty, S. Suri, M. Zhi, M. Li, A. D. Bristow and N. Wu, *J. Am. Chem. Soc.*, 2012, **134**, 15033–15041.
- 25 Z. W. Seh, S. Liu, M. Low, S. Y. Zhang, Z. Liu, A. Mlayah and M. Y. Han, *Adv. Mater.*, 2012, **24**, 2310–2314.
- 26 F. Sordello and C. Minero, *Appl. Catal., B*, 2015, **163**, 452–458.
- 27 H. Zhang, Q. Zhu, Y. Zhang, Y. Wang, L. Zhao and B. Yu, *Adv. Funct. Mater.*, 2007, **17**, 2766–2771.
- 28 M. Singh, D. Jampaiah, A. E. Kandjani, Y. M. Sabri, E. Della Gaspera, P. Reineck, M. Judd, J. Langley, N. Cox, J. van Embden, E. L. H. Mayes, B. C. Gibson, S. K. Bhargava, R. Ramanathan and V. Bansal, *Nanoscale*, 2018, **10**, 6039–6050.
- 29 L. Sinatra, A. P. LaGrow, W. Peng, A. R. Kirmani, A. Amassian, H. Idriss and O. M. Bakr, *J. Catal.*, 2015, **322**, 109–117.
- 30 A. Wang, X. Li, Y. Zhao, W. Wu, J. Chen and H. Meng, *Powder Technol.*, 2014, **261**, 42–48.
- 31 C. H. Tang, P. H. Hsiao and C. Y. Chen, *Nanoscale Res. Lett.*, 2018, **13**, 312.
- 32 P. H. Hsiao, T. C. Li and C. Y. Chen, *Nanoscale Res. Lett.*, 2019, **14**, 244.
- 33 L. Ma, G. Wang, C. Jiang, H. Bao and Q. Xu, *Appl. Surf. Sci.*, 2018, **430**, 263–272.
- 34 H. Yin, X. Wang, L. Wang, Q. Nie, Y. Zhang and W. Wu, *Mater. Res. Bull.*, 2015, **72**, 176–183.
- 35 H. Xu, S. Ouyang, L. Liu, D. Wang, T. Kako and J. Ye, *Nanotechnology*, 2014, **25**, 165402.
- 36 P. Wang, D. Chen and F. Q. Tang, *Langmuir*, 2006, **22**, 4832–4835.
- 37 Y. Wang, J. Tao, X. Wang, Z. Wang, M. Zhang, G. He and Z. Sun, *Ceram. Int.*, 2017, **43**, 4866–4872.
- 38 J. Cheng, Y. Wang, Y. Xing, M. Shahid and W. Pan, *RSC Adv.*, 2017, **7**, 15330–15336.
- 39 W. Wang, D. Xu, B. Cheng, J. Yu and C. Jiang, *J. Mater. Chem. A*, 2017, **5**, 5020–5029.
- 40 K. Dong, J. He, J. Liu, F. Li, L. Yu, Y. Zhang, X. Zhou and H. Ma, *J. Mater. Sci.*, 2017, **52**, 6754–6766.
- 41 Q. Jiang, L. Li, J. Bi, S. Liang and M. Liu, *Nanomaterials*, 2017, **7**, 24.
- 42 Z. Geng, Y. Zhang, X. Yuan, M. Huo, Y. Zhao, Y. Lu and Y. Qiu, *J. Alloys Compd.*, 2015, **644**, 734–741.
- 43 Y. Li, L. Wang, J. Liang, F. Gao, K. Yin and P. Dai, *Nanoscale Res. Lett.*, 2017, **12**, 531.
- 44 S. Zhang, Z. Liu, M. Ruan, Z. Guo, L. E. W. Zhao, D. Zhao, X. Wu and D. Chen, *Appl. Catal., B*, 2020, 262.
- 45 Z. Li, Q. Yang, C. Chen, Z. Zhang and X. Fang, *Chin. J. Catal.*, 2019, **40**, 875–885.
- 46 Y. X. Lin, W. J. Feng, J. J. Zhang, Z. H. Xue, T. J. Zhao, H. Su, S. I. Hirano, X. H. Li and J. S. Chen, *Angew. Chem., Int. Ed. Engl.*, 2018, **57**, 12563–12566.
- 47 X. Wang, L. Mayrhofer, M. Hofer, S. Estrade, L. Lopez-Conesa, H. Zhou, Y. Lin, F. Peiró, Z. Fan, H. Shen, L. Schaefer, M. Moseler, G. Braeuer and A. Waag, *Adv. Energy Mater.*, 2019, **9**, 1900725.
- 48 S. Wang, L. Li, Z. Zhu, M. Zhao, L. Zhang, N. Zhang, Q. Wu, X. Wang and G. Li, *Small*, 2019, **15**, 1804515.
- 49 R. Yang, Y. Ji, Q. Li, Z. Zhao, R. Zhang, L. Liang, F. Liu, Y. Chen, S. Han, X. Yu and H. Liu, *Appl. Catal., B*, 2019, 256.
- 50 Z. Zeng, Y. Yan, J. Chen, P. Zan, Q. Tian and P. Chen, *Adv. Funct. Mater.*, 2019, **29**, 1806500.
- 51 Y. Su, Z. Zhao, S. Li, F. Liu and Z. Zhang, *Inorg. Chem. Front.*, 2018, **5**, 3074–3081.
- 52 T. Takizawa, T. Watanabe and K. Honda, *J. Phys. Chem. C*, 1978, **82**, 1391–1396.
- 53 X. Zhang, D. Xu, Y. Jia and S. Zhang, *RSC Adv.*, 2017, **7**, 30392–30396.
- 54 X. Zhang, D. Xu, D. Huang, F. Liu, K. Xu, H. Wang and S. Zhang, *J. Am. Ceram. Soc.*, 2017, **100**, 2781–2789.

